A magnetless axial-flux machine for range-extended electric vehicles

Lee, Christopher H.T.; Liu, Chunhua; Chau, K. T.

Article

A Magnetless Axial-Flux Machine for Range-Extended Electric Vehicles

Christopher H. T. Lee *, Chunhua Liu and K. T. Chau

Department of Electrical and Electronic Engineering, The University of Hong Kong, Hong Kong, China;
E-Mails: chualiu@eee.hku.hk (C.L.); ktchau@eee.hku.hk (K.T.C.)

* Author to whom correspondence should be addressed; E-Mail: htlee@eee.hku.hk;
Tel.: +852-2859-8404; Fax: +852-2559-8738.

Abstract: A new magnetless axial-flux doubly-salient DC-field (AF-DSDC) machine is proposed and implemented into the application of a range-extended electric vehicle (RE-EV). By employing the radial active part for the torque production, the proposed machine can produce satisfactory torque density to fulfill the requirements of the RE-EV system. With the support of the 3D finite element method (3D-FEM), the performances of the proposed machine are calculated and compared with the requirements of the typical passenger RE-EV applications. To offer a more comprehensive illustration, the common radial-flux (RF) machines are included for comparison.

1. Introduction

With the ever increasing concerns on energy efficiency and hence environmental protection, the development of electric vehicles (EVs) has been speeding up [1–3]. However, conventional EVs rely merely on the battery as the sole power source, thus, these types of EVs can only be used for short duration trips and are not practical for normal daily usage [4,5]. To extend the range for normal applications, the range-extended EV (RE-EV) which also incorporates an internal combustion engine (ICE) as secondary source has been proposed [6–9].

As the key element of the RE-EV system, electric machines have to offer high efficiency, high power density, high controllability, wide-speed range, and maintenance-free operation [10,11]. To achieve these goals, permanent-magnet (PM) machines have been actively developed [12–15]. However, in recent years, the supply of PM materials has been limited and uneven, leading to soaring material costs [16,17], therefore, advanced magnetless doubly-salient (DS) machines have been gaining more attention [18–20].

Compared with PM machines, the magnetless machines have the definite merit of low material costs, but suffer from lower torque density [21,22]. Meanwhile, the axial-flux (AF) machine, which employs the radial length as the active part for torque production, can further improve its torque density, as compared with its profound radial-flux (RF) counterparts [23–26]. Nevertheless, the concept of implementing the DC-field excitation into the AF-DS machine has rarely been addressed yet.

The purpose of this paper is to newly incorporate the DC-field winding into the AF-DS machine, hence creating a new AF-DSDC machine, purposely for RE-EV applications. The design criteria and operating principles of the proposed machine will be discussed. Its performance will be analyzed by using the 3D finite element method (3D-FEM), and then quantitatively compared with the requirements of typical passenger RE-EV applications. For better illustrative purposes, the profound RF machines, namely the RF-switched reluctance (RF-SR), RF-DSDC and RF-doubly-salient permanent-magnet (RF-DSPM) machines are included for comprehensive comparison.

2. Systems Configuration and Operation Modes

Figure 1 shows the RE-EV system, which applies the in-wheel direct drive architecture. Based on the requirements of a typical passenger RE-EV, the targeted specifications of the system for each of the motors are listed in Table 1 [27,28]. This RE-EV system utilizes the motors as the major power source for the normal operations, while the ICE served as the supplementary part for range extension. Basically, the proposed RE-EV system can offer four major operation modes.

Figure 1. Range-extended electric vehicle (RE-EV) system. ICE: internal combustion engine; DC: direct current; and AC: alternating current.
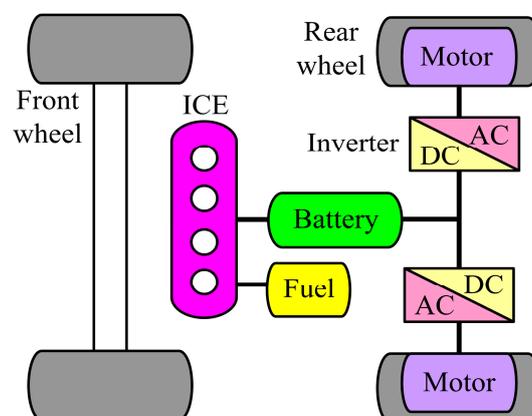
Table 1. Targeted motor specifications for the RE-EV system.

Item	Value	Unit
Peak DC voltage	360	V
Rated power	4.7	kW
Rated torque	150	Nm
Constant-torque operation	0–300	rpm
Constant-power operation	300–900	rpm
Peak torque	130% for 10 s	-
Wheel dimension	195/65 R15	-

2.1. Mode 1: Torque Boosting

When the RE-EV needs to accelerate or run uphill, the motor has to operate with the torque boosting mode, namely, the motor is requested to output the peak torque under a short period of time. Under this mode, the current density of the DC-field excitation is purposely boosted up to strengthen the flux densities, resulting in the maximized output torque.

2.2. Mode 2: Flux-Weakening Operation

After the RE-EV has started up with the torque boosting mode, the generated electromotive force (EMF) among the armature windings starts to increase with the increased operating speed. In order to maintain a certain power level within the constant power operation region, the flux density should be weakened accordingly. By regulating the independent DC-field excitation, the proposed RE-EV system can effectively achieve this flux-weakening operation. Theoretically, RE-EVs can provide infinite speed ranges by regulating the DC-field excitations [18,19].

2.3. Mode 3: Fault-Tolerant Operation

Whilst the DC-field winding is under open-circuit fault or short-circuit fault conditions, the DC-field current should be cut off and the proposed motor can still be operated by the remaining sets of healthy armature winding [29]. Once the DC-field current has malfunctioned, the remaining armature current can be purposely boosted up and operated with the unipolar conduction scheme, such that the torque level can be maintained. Meanwhile, by employing the profound fault-tolerant operating algorithms, the proposed machine can also achieve the fault-tolerant operation under the armature winding fault [29]. This fault-tolerant operation is very important for RE-EVs as it can avoid traffic jams or even fatal accidents when the machine suddenly malfunctions due to a fault.

2.4. Mode 4: Battery Charging

Once the battery is almost exhausted, the ICE can be applied to operate the RE-EV and to charge the battery for range extension. As the engine speed varies along with the wide range of vehicle speeds, the generated voltage is varying accordingly. Meanwhile, when the RE-EV runs downhill or in braking occasions, the motor undergoes a regenerative braking stage and starts to charge the battery [14]. This time-varying generated voltage may overcharge the battery and shorten its life cycle. In order to

extend the battery life, the proposed motor can control its DC-field winding, leading to regulation of the flux density in a way that the generated voltage is kept as constant as possible.

3. Proposed Axial-Flux Doubly-Salient DC-Field (AF-DSDC) Machine

3.1. Proposed Machine Structure

Figure 2 shows the topology of the proposed 8/10-pole AF-DSDC machine, which consists of a double-sided-stator sandwiched-rotor structure. The stator and rotor construction of the proposed machine are similar to those of other conventional AF machines [23].

Figure 2. Proposed axial-flux doubly-salient DC-field (AF-DSDC) machine.
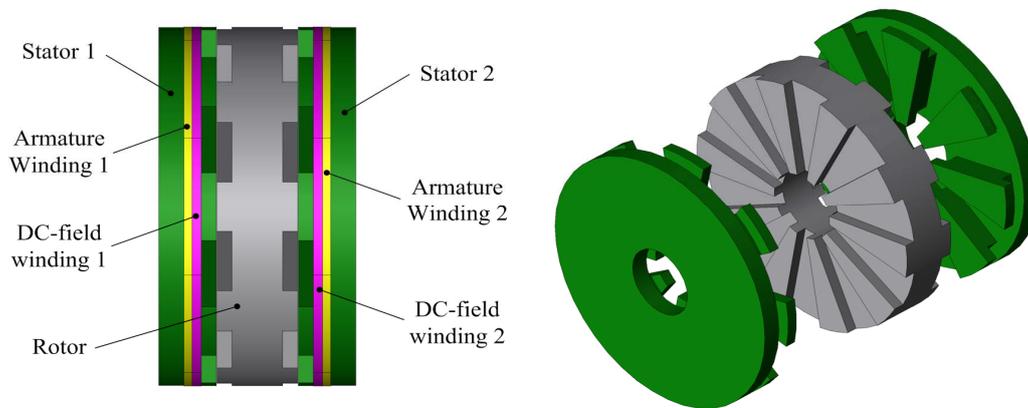
Based on this structure and accompanied by the proper dimensions, the proposed machine is able to mount its rotor to the tire directly, such that in-wheel motor drive can be achieved instinctively as shown in Figure 3.

Figure 3. In-wheel direct drive internal structure.
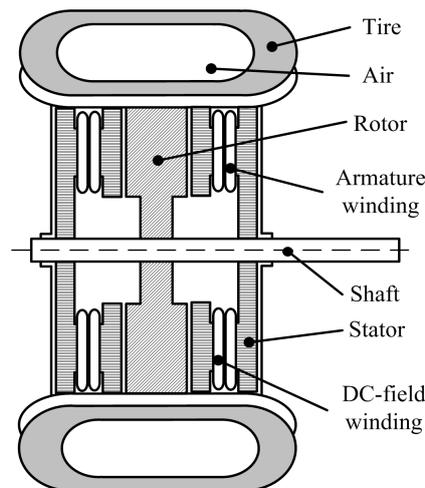
The proposed machine is designed based on the four-phase topology due to considerations of stability and cost-effectiveness. The corresponding key design data are tabulated in Table 2. Meanwhile, the proposed AF-DSDC machine employs its radial part for torque production and hence its torque density is improved compared with its RF counterparts [23–26].

Table 2. Key data of proposed machine.

Item	AF-DSDC	Unit
Radial outside diameter	381	mm
Radial inside diameter	100	mm
Axial stack length	195	mm
Air-gap length of both segments	0.5	mm
Number of stator poles of both segments	8	-
Number of rotor poles of both segments	10	-
Number of armature phases	4	-
Number of turns per armature coil	50	-
Rotor and stator material	Steel sheet: 50JN700 (JFE Steel Corporation, Tokyo, Japan)	-
Armature and DC-field winding material	Copper	-

Since the AF-DSDC machine is derived from the conventional RF-DSDC machine, its design equations such as the pole arrangement [22] can be extended from that of the profound RF-DSDC machine. Thus, the pole arrangements for the AF-DSDC are governed by:

$$\begin{cases} N_s = 2mk \\ N_r = N_s \pm 2k \end{cases} \tag{1}$$

where N_s is the number of stator poles; N_r is the number of rotor poles; m is the number of armature phases; and k is any integer. By selecting $m = 4$ and $k = 1$, this ends up with $N_s = 8$ and $N_r = 10$, resulting with the proposed structure for the AF-DSDC machine.

3.2. DC Flux-Linkage Pattern

The proposed AF-DSDC machine uses two types of winding, namely the DC-field winding and armature winding, in each of its sided-stators, and both sets of winding adopt the concentrated winding arrangement. With this configuration, each of the two sets of winding is installed with their magnetic axes parallel to each other, albeit in opposing directions. These lead to the fact that the flux in the rotor yoke is divided into two equal paths as shown in Figure 4.

Figure 4. DC flux-linkage paths of the proposed machine: (**a**) Position 1; and (**b**) Position 2.
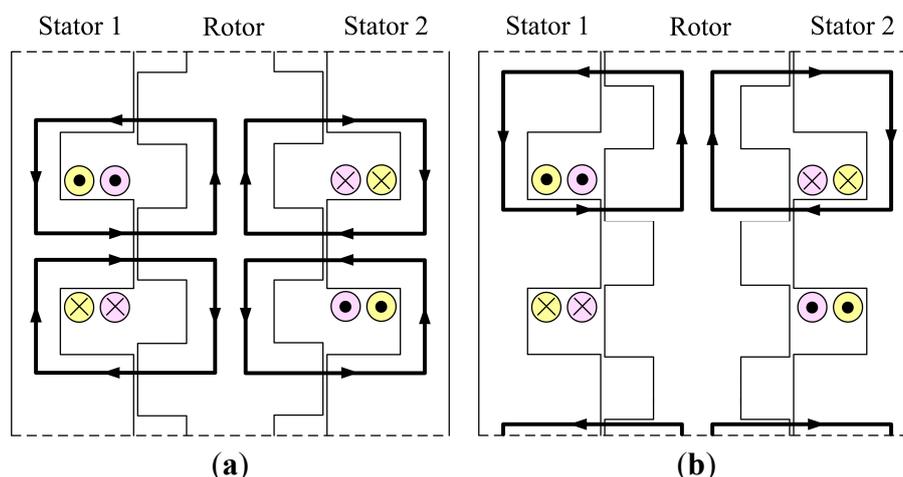
Since the machine has a symmetrical structure, the torques produced by the two sided-stators are complementary with each other, leading to a balanced resultant torque. In addition, to simplify the operation complexity, each of the corresponding sets of windings in the two sided-stators can be purposely connected in series.

3.3. Operation Principles

With the additional DC-field excitation, the proposed AF-DSDC machine can be operated at two different conduction schemes, namely the bipolar conduction scheme and unipolar conduction scheme. To be specific, the bipolar conduction scheme mainly serves for normal operations, whereas the unipolar conduction scheme is devoted to fault-tolerant operation [19]. A full-bridge inverter is installed for the armature winding, providing independent phase control capability. Meanwhile, a full-bridge DC-DC converter is installed for the DC-field winding, resulting in flux strengthening and weakening abilities [14].

3.3.1. Bipolar Conduction Scheme

When the DC-field excitation is available, the proposed AF-DSDC machine can be operated by using the bipolar conduction scheme, which is similar to the conventional RF-DSPM machine operation [13,14]. When the DC flux-linkage Ψ_{DC} is increasing and the no-load EMF is positive, a positive armature current I_{BLDC} is applied to produce a positive torque T_{DC}. Similarly, a negative armature current $-I_{BLDC}$ is applied when the Ψ_{DC} is decreasing and the no-load EMF is negative, hence also producing a positive torque. The operating waveforms under the bipolar conduction scheme are shown in Figure 5a.

Figure 5. Operation principle schemes: (**a**) bipolar conduction; and (**b**) unipolar conduction.

(**a**)   (**b**)
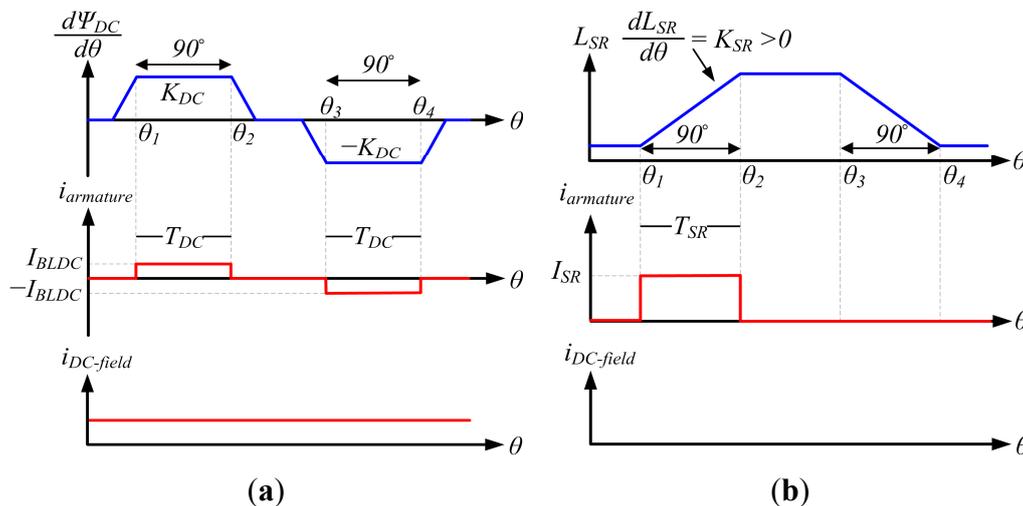
Each phase performs 90° conduction with $\theta_2 - \theta_1 = \theta_4 - \theta_3 = 90°$. The resulting electromagnetic torque T_{DC} can be expressed as:

$$T_{DC} = \frac{1}{2\pi} \int_0^{2\pi} \left(i_{BLDC} \frac{d\psi_{DC}}{d\theta} + \frac{1}{2} i_{BLDC}^2 \frac{dL_D}{d\theta} \right) d\theta \tag{2}$$

where L_D is the self-inductance. Under this conduction scheme, the torque is majorly constituted by the DC-field torque component, whereas the reluctance torque component is small and pulsates with a zero

average value [13,14]. Hence, after neglecting the pulsation torque component, the torque equation can be further expressed as:

$$T_{DC} = \frac{1}{2\pi}\left(\int_{\theta_1}^{\theta_2} I_{BLDC}K_{DC}d\theta + \int_{\theta_3}^{\theta_4}\left(-I_{BLDC}\right)\left(-K_{DC}\right)d\theta \right) = \frac{1}{2}I_{BLDC}K_{DC} \tag{3}$$

and K_{DC} is the slope of Ψ_{DC} with respect to θ.

3.3.2. Unipolar Conduction Scheme

Whilst the DC-field winding is under any fault condition, the DC-field current should be cut off and the proposed machine can then be operated by using the unipolar conduction scheme, which is similar as the RF-SR machine [19,22]. Namely, a unipolar rectangular current I_{SR} is fed to the armature winding during the increasing period of the self-inductance L_{SR}, resulting as the positive corresponding reluctance torque T_{SR} within $\theta_2 - \theta_1 = 90°$ as shown in Figure 5b. However, under this conduction scheme, only half of the torque producing period is utilized, and thus the torque performance is degraded and the torque ripple is larger than that under the bipolar conduction operation conditions. Therefore, this mode is regarded as the fault-tolerant operation [29] for the scenario when the DC-field winding is under fault condition. The reluctance torque at this unipolar conduction scheme can be expressed as:

$$T_{SR} = \frac{1}{2\pi}\int_0^{2\pi}\left(\frac{1}{2}i_{SR}^2\frac{dL_{SR}}{d\theta} \right)d\theta = \frac{1}{2\pi}\int_{\theta_1}^{\theta_2}\left(\frac{1}{2}I_{SR}^2K_{SR} \right)d\theta = \frac{1}{8}I_{SR}^2K_{SR} \tag{4}$$

where K_{SR} is the slope of L_{SR} with respect to θ. In order to maintain the same torque level at both modes, the Equations (3) and (4) should be equated to yield:

$$I_{SR} = 2\sqrt{\frac{I_{BLDC}K_{DC}}{K_{SR}}} \tag{5}$$

Based on Equation (5), the armature current at the unipolar conduction scheme can be deduced, which enables the proposed machine to offer the same average torque as that at the bipolar conduction scheme. However, the unipolar conduction scheme generally requires a larger armature current, which is not suitable for normal operations. In addition, this operation scheme utilizes only half of the torque producing period, therefore, the corresponding torque ripple is worse than that under the bipolar conduction scheme.

4. Electromagnetic Field Analysis

Electromagnetic field analysis has been widely applied for the design of electric machines, and it can be basically categorized as the analytical field calculation [30] and the numerical field calculation [31]. In this paper, 3D-FEM is employed for the analysis of the proposed AF-DSDC machine performance [24,30]. The magnetic solver used to perform the finite element analysis for the proposed machines is the JMAG-Designer and each simulation process takes more than 10 h using a high-performance PC. Figure 6 shows the corresponding no-load magnetic field distributions of the proposed machine. It can be shown that the magnetic flux in the rotor yoke is divided into two

symmetrical patterns via the two sided-stators. Hence, it can be predicted that the two individual torques produced by the two segments are identical.

Figure 6. No-load magnetic field distributions: (**a**) Position 1; and (**b**) Position 2.
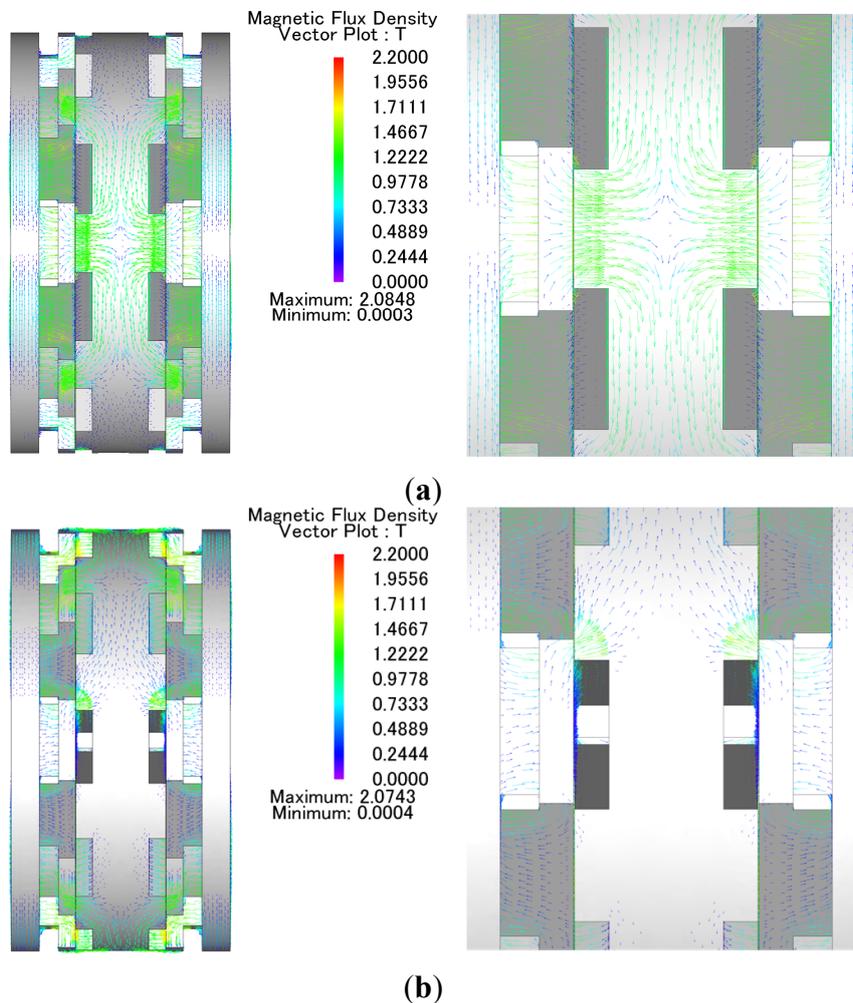

(**a**)

(**b**)

Figure 7 shows the air-gap flux density waveforms of both air-gaps of the proposed machine under the no-load condition where the DC-field excitation is under the rated current densities of 5 A/mm^2. These show that both air-gaps achieve the same flux pattern. Hence, it can be confirmed that under the same electric supply, the output torques produced by the two sided-stators should be the same.

Figure 7. Air-gap flux density waveforms: (**a**) Air-gap 1; and (**b**) Air-gap 2.

(**a**)

(**b**)
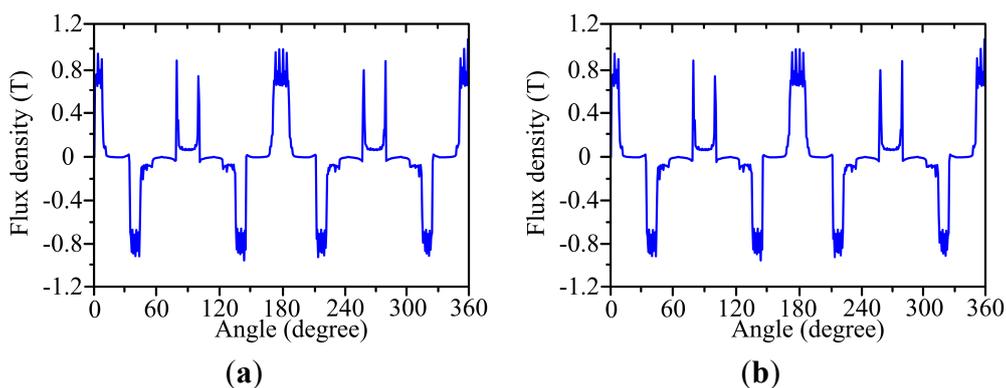
Figures 8 and 9 show the DC flux-linkage waveforms for the bipolar conduction scheme (with the DC-field excitation set at 5 A/mm^2) and the self-inductance waveforms for the unipolar conduction scheme (without any DC-field excitation), respectively.

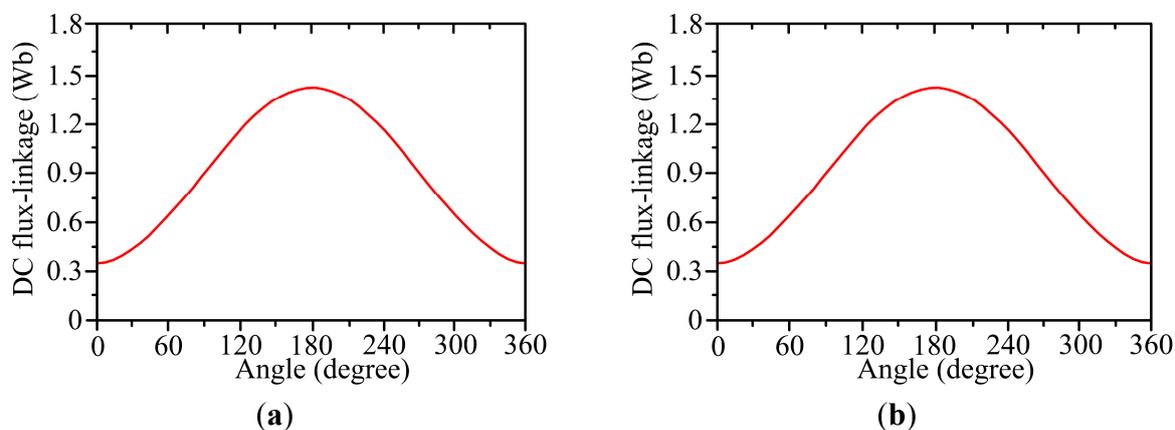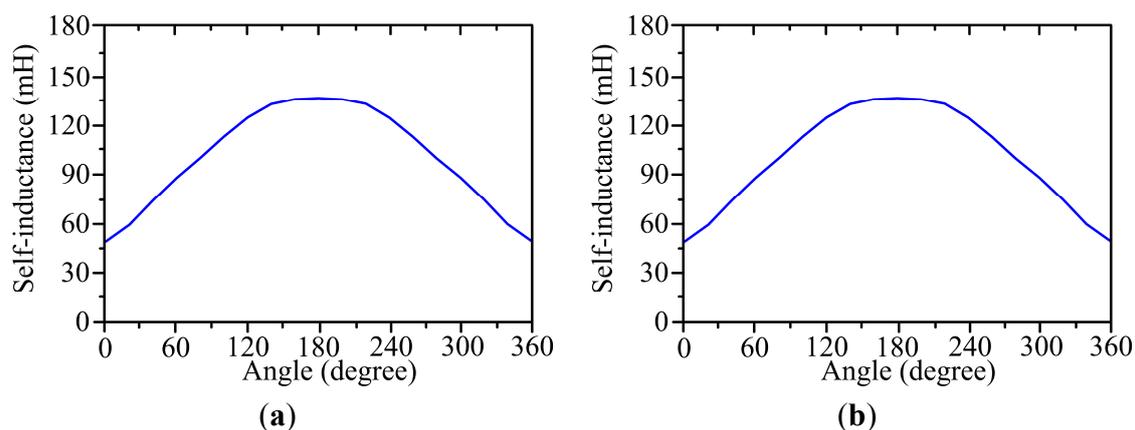**Figure 8.** DC flux-linkage waveforms: (**a**) Winding 1; and (**b**) Winding 2.

(**a**)   (**b**)

Figure 9. Self-inductance waveforms: (**a**) Winding 1; and (**b**) Winding 2.

(**a**)   (**b**)

In order to maintain the same torque level between both conduction schemes, the armature current at the unipolar one is given by Equation (5) in which the values of K_{DC}, and K_{SR} can be deduced from Figures 8 and 9, as summarized in Table 3. As calculated, in the unipolar conduction mode, the armature currents have to be boosted by approximately 129%, as compared with the bipolar conduction mode. At this current density range, the machine can still be operated for a relatively long period of time, say several hours, without thermal damage.

Table 3. Key parameters at different conduction schemes.

| Item	Winding 1	Winding 2
Rated current at bipolar conduction	10 A	10 A
Slope of DC flux-linkage K_{DC}	1.04	1.04
Slope of self-inductance K_{SR}	0.079	0.079
Rated current at unipolar conduction	22.9 A	22.9 A

5. Performance Analysis

5.1. No-Load EMF Waveforms at Rated Conditions

By using 3D-FEM, the performance of the proposed machine can be thoroughly analyzed. Firstly, the no-load EMF waveforms at the base speed 300 rpm with the rated DC-field excitation of 5 A/mm^2 are simulated as shown in Figure 10. It can be seen that the no-load EMF waveforms of both sets of windings have the balanced four-phase patterns. These confirm that the setting of the pole-pair arrangement and the winding configurations are correct. In addition, the results show that both no-load EMF waveforms provide the same polarities and values, and both of them can achieve up to a peak value of 153 V. Hence, even when both sets of armature winding are connected in series, the targeted DC supply voltage is still able to support normal operation.

Figure 10. No-load electromotive force (EMF) waveforms at rated conditions: (**a**) Winding 1; and (**b**) Winding 2.
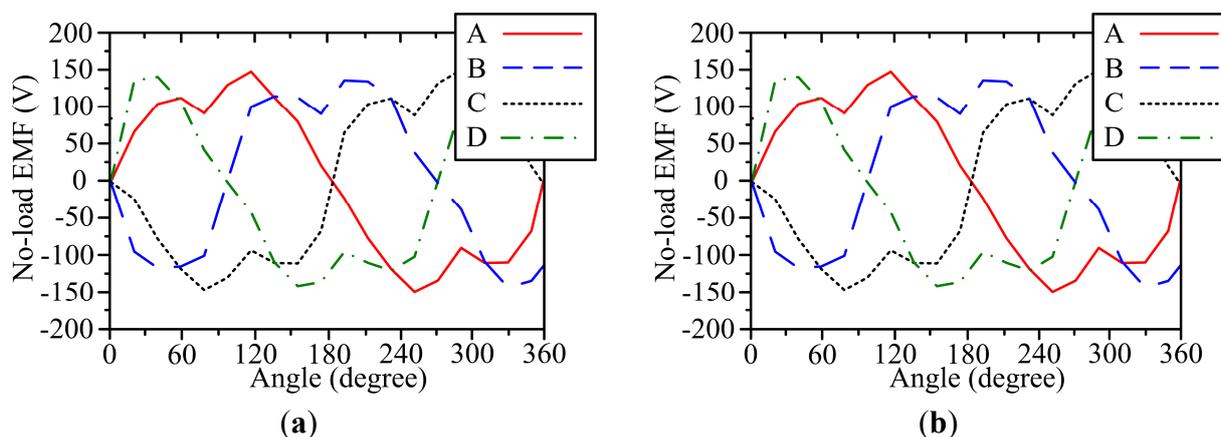
5.2. Performance of Mode 1—Torque Boosting

Secondly, Figure 11 shows the torque performances of the proposed machine at rated DC-field excitation (5 A/mm^2) and at strengthened DC-field excitation (10 A/mm^2), respectively. Since the independent DC-field winding can be controlled effectively, it can be utilized to regulate the air-gap flux densities to fit different situations. It can be observed that the average steady torques of the machine at rated and at strengthened DC-field excitation are 154.2 Nm and 203.2 Nm, respectively. These confirm that the proposed machine can fulfill the torque requirements of normal operation, including the *Mode 1*, the torque boosting mode. Consequently, the torque ripples at rated and at strengthened DC-field excitation can be found to be 27.4% and 43.2%, respectively, which are both very acceptable for normal RE-EV applications [13,28].

Thirdly, the cogging torque waveforms of the proposed machine at rated and strengthened DC-field excitations are simulated as shown in Figure 12. It can be found that the peak values at rated and strengthened DC-field excitations are 18.6 Nm and 42.4 Nm, respectively. As compared with the corresponding average torques, they are only 12.1% and 20.9%, respectively, which are also comparable to those of conventional RF-DSPM machines [13].

Figure 11. Torque waveforms at bipolar conduction scheme: (**a**) rated DC-field excitation; and (**b**) strengthened DC-field excitation.
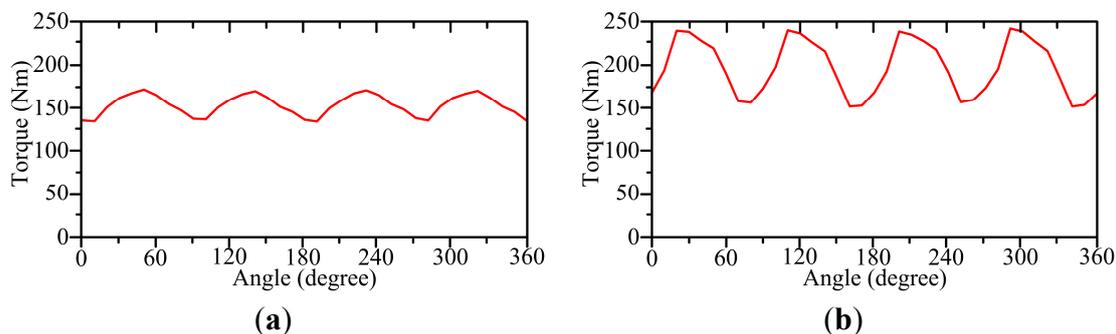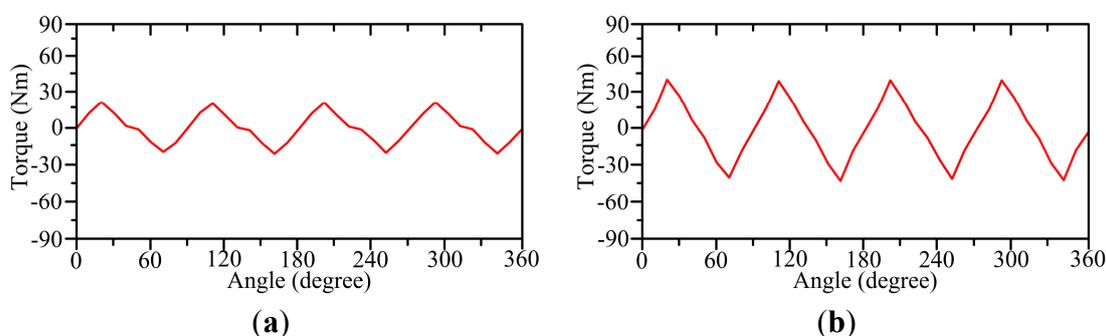

(**a**)

(**b**)

Figure 12. Cogging torque waveforms at bipolar conduction scheme: (**a**) rated DC-field excitation; and (**b**) strengthened DC-field excitation.

(**a**)

(**b**)

5.3. Performance of Mode 2—Flux-Weakening Operation

Fourthly, the torque-speed characteristics of the proposed machine are simulated and shown in Figure 13. The DC-field excitation can be independently controlled easily and hence, the proposed machine can achieve high flux-weakening capabilities for wide-speed range operations, which is one of the major criteria for RE-EV applications. The result confirms that the proposed machine can maintain constant power characteristics over the wide range of speeds. Particularly, with the DC-field excitations set at 1.5 A/mm^2, the operating speed of the proposed machine is approximately 907 rpm. The result can cover the whole targeted speed range and fulfill the requirements of the *Mode 2*, the flux-weakening operation.

Figure 13. Torque-speed characteristics of the proposed machine.
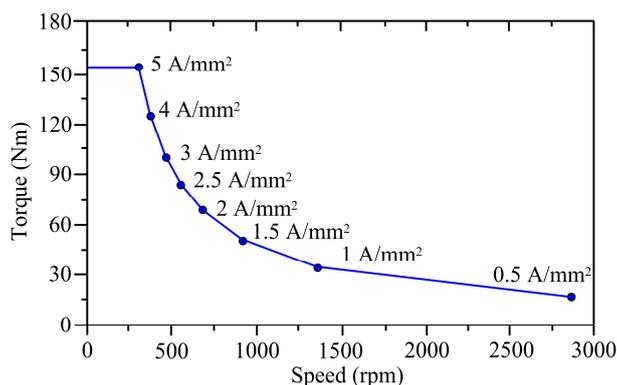
5.4. Performance of Mode 3—Fault-Tolerant Operation

Fifthly, when the DC-field excitation is cut off, the proposed machine can be operated with the unipolar conduction scheme and the corresponding torque performance is shown in Figure 14. The averaged torque and the torque ripple under the unipolar conduction scheme are 148.2 Nm and 40.1%, respectively. These confirm that even if DC-field excitation malfunctions, the proposed machine can still offer the same torque level for normal operation under the unipolar conduction scheme. Meanwhile, because only half of the torque producing zone is utilized, the torque ripple and the armature current densities are higher than those of the bipolar conduction operation. Furthermore, the efficiency at the fault-tolerant mode is lower than that of the normal operation mode. Hence, the unipolar operation should only be adopted for the *Mode 3*, fault-tolerant operation.

Figure 14. Torque waveforms under the unipolar conduction scheme.
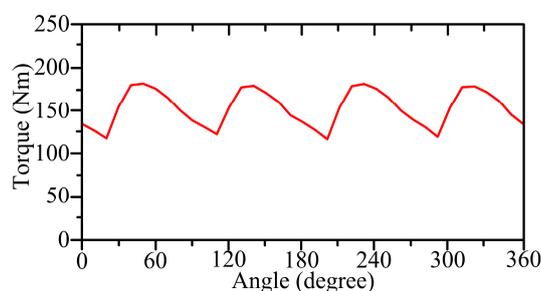
5.5. Performance of Mode 4—Battery Charging

Finally, Figure 15 shows the no-load EMF waveforms at various speeds under two situations, namely without and with flux regulation operations, respectively. Obviously, without any DC-field control, the amplitudes of the output voltages vary with the operating speeds. This unstable generated voltage is not favorable for charging the battery. Meanwhile, by purposely tuning the DC-field excitation, the output voltages can be kept constant over a wide range of speeds in order to fulfill the expectation of the *Mode 4*, the battery charging mode.

Figure 15. No-load EMF waveforms at various speeds: (**a**) without flux regulation; and (**b**) with flux regulation.
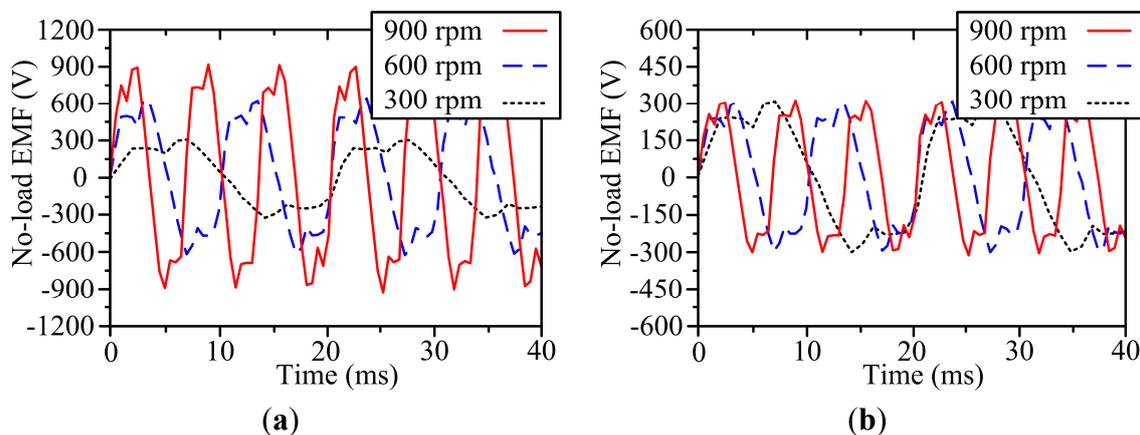
6. Comparisons among RF Machines

The performances of the proposed AF-DSDC machine are thoroughly analyzed by 3D-FEM, and summarized in Table 4.

Table 4. Proposed AF-DSDC machine performances.

Item	Bipolar conduction	Unipolar conduction
Rated Power	4.8 kW	4.6 kW
Power density	35.4 W/kg	33.8 W/kg
Operating frequency at base speed	50 Hz	50 Hz
No-load EMF of Winding 1	153 V	N/A
No-load EMF of Winding 2	153 V	N/A
Rated DC-field excitation	5 A/mm^2	N/A
Rated torque	154.2 Nm	148.2 Nm
Torque ripple at rated torque	27.4%	40.1%
Cogging torque at rated torque	18.6 Nm	N/A
% Cogging torque at rated torque	12.1%	N/A
Boosted DC-field excitation	10 A/mm^2	N/A
Boosted torque	203.2 Nm	N/A
Torque ripple at boosted torque	43.2%	N/A
Cogging torque at boosted torque	42.4 Nm	N/A
% Cogging torque at boosted torque	20.9%	N/A

Meanwhile, to further illustrate the merits of the proposed AF-DSDC machine, the profound RF machines, namely the RF-SR, RF-DSDC and RF-DSPM are also included [2,11,13], and as shown in Figure 16a–c, respectively. To have a fair comparison, all machines have the same machine dimensions, namely the radial outside diameters, radial inside diameters, axial stack lengths, and air-gap lengths. In addition, the winding factors and current densities are also equalized.

Figure 16. Radial-flux (RF) machines: (**a**) RF-switched reluctance (RF-SR); (**b**) RF-doubly-salient DC-field (RF-DSDC); and (**c**) RF-doubly-salient permanent-magnet (RF-DSPM).

(**a**)

Figure 16. *Cont.*

(**b**)

(**c**)
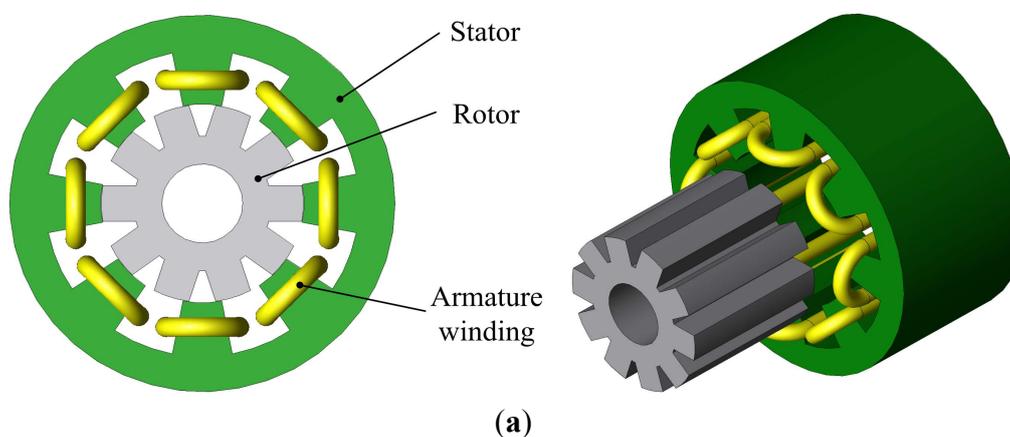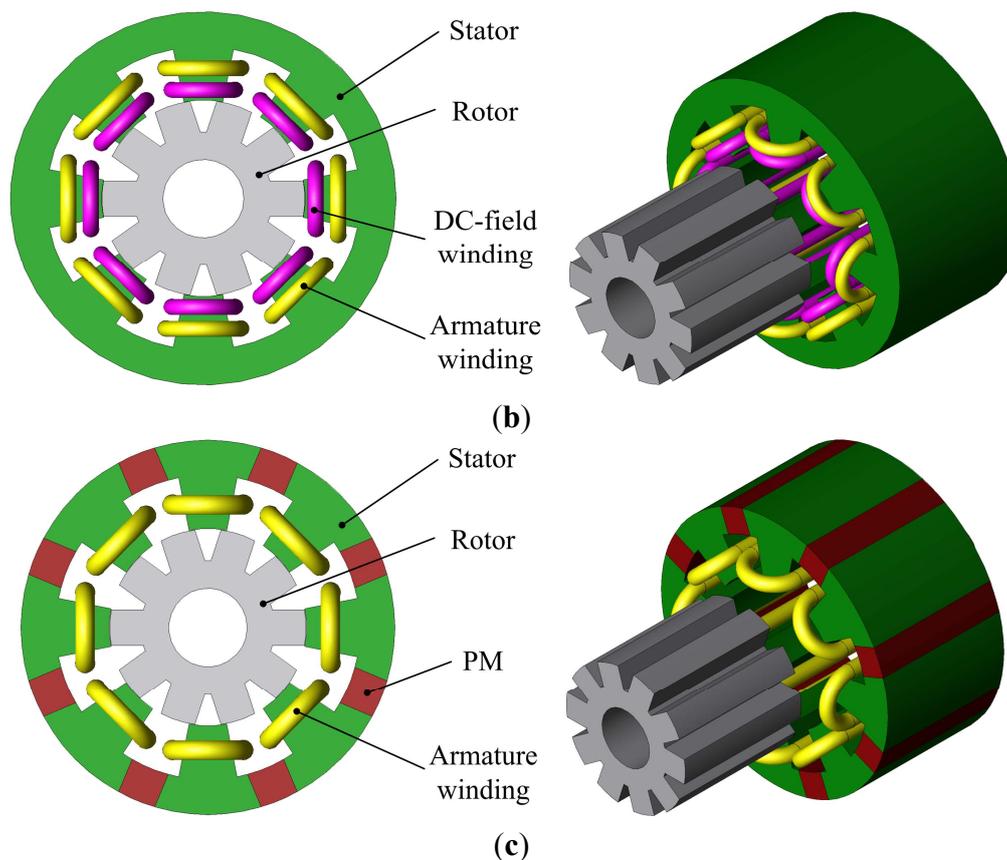
Based on the FEM, the performances of the RF machines are calculated and summarized in Table 5. As expected, the magnetless RF-SR uses only half of its torque producing period, leading to the worst performance in terms of the gravimetric and volumetric rated torque densities. Meanwhile, by utilizing all the torque producing periods, the RF-DSDC can offer better torque performances than the RF-SR machine. With the application of the radial part for torque production, the proposed AF-DSDC machine can offer much higher torque densities than the profound magnetless RF counterparts, and is comparable with the RF-DSPM.

Table 5. Axial-flux (AF) and RF machine performance comparisons.

Item	RF-SR	RF-DSDC	RF-DSPM	AF-DSDC
Rated torque/mass	0.51 Nm/kg	0.61 Nm/kg	1.21 Nm/kg	1.13 Nm/kg
Rated torque/volume	4.12 kNm/m^3	4.85 kNm/m^3	9.51 kNm/m^3	8.97 kNm/m^3
Material cost	208.4 USD	209.8 USD	411.9 USD	239.5 USD
Rated torque/cost	0.34 Nm/USD	0.41 Nm/USD	0.39 Nm/USD	0.65 Nm/USD

Even though the RF-DSPM machine provides the highest torque densities and outperforms its magnetless counterparts, the supply of the PM materials is limited and irregular, resulting to the surged materials cost [17]. To increase the market penetration of the RE-EV adoptions, the concept of the cost-effectiveness should also be considered. The materials costs of the machines are calculated based on the current market prices of the raw materials. Without any installation of PM materials, the proposed AF-DSDC machine achieves the best performance regarding cost-effectiveness among all the counterparts,

and thus is particularly favorable for RE-EV applications. Meanwhile, discussions on the efficiency maps of all machines will be included in our future papers.

7. Conclusions

In this paper, a new magnetless AF-DSDC machine has been proposed and implemented for RE-EV applications. By adopting the radial active part for torque production, the proposed AF-DSDC machine offers better performance than its conventional RF counterparts do, especially from a cost-effectiveness perspective. The AF-DSDC machine is under prototyping and the experimental data will be the substance of our future papers. With the support of the external DC-field winding, the proposed machine can accomplish different operation modes, namely the torque boosting, flux-weakening, fault-tolerant and battery charging modes. Hence, it is anticipated that the proposed machine will have great potential for implementation into RE-EV systems.

Acknowledgments

Conflicts of Interest

The authors declare no conflict of interest.

References

1. Ehsani, M.; Rahman, K.M.; Toliyat, H.A. Propulsion system design of electric and hybrid vehicles. *IEEE Trans. Ind. Electron.* **1997**, *44*, 19–27.
2. Zhu, Z.Q.; Howe, D. Electrical machines and drives for electric, hybrid and fuel cell vehicles. *IEEE Proc.* **2007**, *95*, 746–756.
3. Chau, K.T.; Chan, C.C.; Liu, C. Overview of permanent-magnet brushless drives for electric and hybrid electric vehicles. *IEEE Trans. Ind. Electron.* **2008**, *55*, 2246–2257.
4. Hermance, D.; Sasaki, S. Hybrid electric vehicles take to the streets. *IEEE Spectr.* **1998**, *35*, 48–52.
5. Chan, C.C. The state of the art of electric and hybrid vehicles. *IEEE Proc.* **2002**, *90*, 247–275.
6. Ehsani, M.; Gao, Y.; Miller, J.M. Hybrid electric vehicles: Architecture and motor drives. *IEEE Proc.* **2007**, *95*, 719–728.
7. Chau, K.T.; Chan, C.C. Emerging energy-efficient technologies for hybrid electric vehicles. *IEEE Proc.* **2007**, *95*, 821–835.
8. Van Wieringen, M.; Pop-Iliev, R. Development of a dual-fuel power generation system for an extended range plug-in hybrid electric vehicle. *IEEE Trans. Ind. Electron.* **2010**, *57*, 641–648.
9. Ott, T.; Onder, C.; Guzzella, L. Hybrid-electric vehicle with natural gas-diesel engine. *Energies* **2013**, *6*, 3571–3592.
10. Cheng, M.; Hua, W.; Zhang, J.; Zhao, W. Overview of stator-permanent magnet brushless machines. *IEEE Trans. Ind. Electron.* **2011**, *58*, 5087–5101.

11. Chau, K.T.; Li, W.; Lee, C.H.T. Challenges and opportunities of electric machines for renewable energy. *Prog. Electromagn. Res. B* **2012**, *42*, 45–74.

12. Liu, C.; Chau, K.T.; Jiang, J.Z.; Niu, S. Comparison of stator-permanent-magnet brushless machines. *IEEE Trans. Magn.* **2008**, *44*, 4405–4408.

13. Zhang, J.; Cheng, M.; Chen, Z.; Hua, W. Comparison of stator-mounted permanent-magnet machines based on a general power equations. *IEEE Trans. Energy Convers.* **2009**, *24*, 826–834.

14. Liu, C.; Chau, K.T.; Jiang, J.Z. A permanent-magnet hybrid brushless integrated starter-generator for hybrid electric vehicles. *IEEE Trans. Ind. Electron.* **2010**, *57*, 4055–4064.

15. Zheng, P.; Wu, F.; Lei, Y.; Sui, Y.; Yu, B. Investigation of a novel 24-slot/14-pole six-phase fault-tolerant modular permanent-magnet in-wheel motor for electric vehicles. *Energies* **2013**, *6*, 4980–5002.

16. Li, J.; Chau, K.T. Performance and cost comparison of permanent-magnet Vernier machines. *IEEE Trans. Appl. Supercond.* **2012**, *22*, doi:10.1109/TASC.2011.2180009.

17. Chen, M.; Chau, K.T.; Li, W.; Liu, C. Cost-effectiveness comparison of coaxial magnetic gears with different magnet materials. *IEEE Trans. Magn.* **2014**, *50*, doi:10.1109/TMAG.2013.2281988.

18. Liu, C.; Chau, K.T.; Zhong, J.; Li, J. Design and analysis of a HTS brushless doubly-fed doubly salient machine. *IEEE Trans. Appl. Supercond.* **2011**, *21*, 1119–1122.

19. Lee, C.H.T.; Chau, K.T.; Liu, C. Electromagnetic design and analysis of magnetless double-rotor dual-mode machines. *Prog. Electromagn. Res.* **2013**, *142*, 333–351.

20. Lee, C.H.T.; Chau, K.T.; Liu, C. Design and analysis of a new multitoothed magnetless doubly-salient machine. *IEEE Trans. Appl. Supercond.* **2014**, *24*, doi:10.1109/TASC.2013.2286742.

21. Zhu, Z.Q. Switched Flux Permanent Magnet Machines-Innovation Continues. In Proceedings of the International Conference on Electrical Machines and Systems (ICEMS), Beijing, China, 20–23 August 2011; pp. 1–10.

22. Lee, C.H.T.; Chau, K.T.; Liu, C.; Wu, D.; Gao, S. Quantitative comparison and analysis of magnetless machine with reluctance topologies. *IEEE Trans. Magn.* **2013**, *49*, 3969–3972.

23. Profumo, F.; Zhang, Z.; Tenconi, A. Axial flux machines drives: A new viable solution for electric cars. *IEEE Trans. Ind. Electron.* **1997**, *44*, 39–45.

24. Ho, S.L.; Niu, S.; Fu, W.N. Design and analysis of a novel axial-flux electric machine. *IEEE Trans. Magn.* **2011**, *47*, 4368–4371.

25. Madhavan, R.; Fernandes, B.G. Axial flux segmented SRM with a higher number of rotor segments for electric vehicles. *IEEE Trans. Energy Convers.* **2013**, *28*, 203–213.

26. Zheng, P.; Song, Z.; Bai, J.; Tong, C.; Yu, B. Research on an axial magnetic-field-modulated brushless double rotor machine. *Energies* **2013**, *6*, 4799–4829.

27. Olszewski, M. *Evaluation of the 2010 Toyota Prius Hybrid Synergy Drive System*; Oak Ridge National Laboratory (ORNL), U.S. Department Energy: Washington, DC, USA, 2011.

28. Cao, R.; Mi, C.; Cheng, M. Quantitative comparison of flux-switching permanent-magnet motors with interior permanent magnet motor for EV, HEV, and PHEV applications. *IEEE Trans. Magn.* **2012**, *48*, 2374–2384.

29. Yu, C.; Chau, K.T. New fault-tolerant flux-mnemonic doubly-salient permanent-magnet motor drive. *IET Electr. Power Appl.* **2011**, *5*, 393–403.

30. Zheng, P.; Zhao, Q.; Bai, J.; Yu, B.; Song, Z.; Shang, J. Analysis and design of a transverse-flux dual rotor machine for power-split hybrid electric vehicle applications. *Energies* **2013**, *6*, 6548–6568.
31. Wang, Y.; Chau, K.T.; Chan, C.C.; Jiang, J.Z. Transient analysis of a new outer-rotor permanent-magnet brushless dc drive using circuit-field-torque coupled time-stepping finite-element method. *IEEE Trans. Magn.* **2002**, *38*, 1297–1300.